

angle with each other. When a human-driven vehicle is equipped with a V2X device we refer to it as a connected human-driven vehicle (CHV), while when the vehicle is automated we refer to it as a connected automated vehicle (CAV).

For high penetrations of CAVs, the benefits of connectivity are clear. Motion coordination of CAVs in vehicle platoons [7], lane change maneuvers [8] and highway merges [9], [10] can be accomplished, which leads to smooth traffic flow without congestion. However, in the near future, the penetration of CAVs is expected to remain low, while the penetration of CHVs is expected to increase significantly. Hence, a CAV may utilize V2V information from nearby CHVs to make decisions and to plan and control its motion [11], [12]. In our study, the CAV performs communication-based longitudinal control, often referred to as connected cruise control (CCC) [13], and this is augmented with communication-based lateral control. Both controllers utilize V2V communication similarly to the scenario investigated in [14], where numerical simulations were applied to a simplified vehicle model without taking into account the time delay in the control loops. Here, we present both theoretical and experimental results while utilizing advanced mechanical models and demonstrate the robustness of the designed controllers against time delay.

To demonstrate the feasibility of V2X communication-based motion control, in this paper, we focus on developing controllers for CAVs that can utilize V2V information from a CHV ahead in highway driving scenarios; see Fig. 1. We demonstrate both theoretically and experimentally the feasibility of controlling a CAV based on the received data when information from optical sensors is not available. We take into account the delay arising from intermittent communication, on-board computation, state estimation, and actuation [15]. The corresponding longitudinal and lateral controllers are designed to be robust against delays, and their performance is validated experimentally using a real CAV and a CHV. We introduce performance metrics that quantify stability and disturbance attenuation properties based on the experimentally recorded time signals. These metrics are used to verify the theoretical results and to fine tune controllers. The combined application of the longitudinal and lateral controllers is tested by performing lane changes while following a CHV; similar to the one in Fig. 1(b) that was accomplished by a human driver.

The rest of the paper is organized as follows. In Section II the architecture of the controller is laid out and the test environment is described. The longitudinal and lateral control designs are shown in Sections III and IV, respectively. The experimental results showcasing the combined performance of the controllers are presented in Section V. Finally, we conclude our results and lay out future research directions in Section VI.

II. CONTROL STRATEGY AND EXPERIMENTAL SETUP

In this section, we describe our control strategy aimed at highway driving scenarios. The physical layout of the connected vehicle system is explained and the key quantities obtained via GPS sensors and V2X communication are spelled out. Also, we

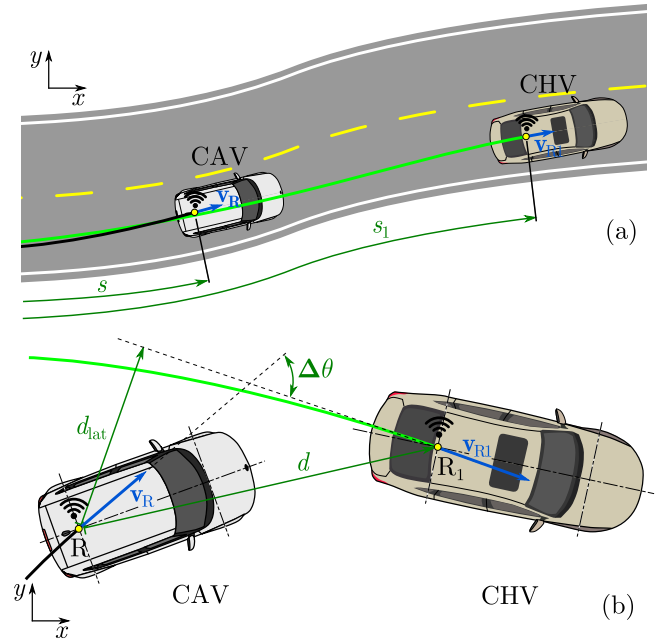


Fig. 2. The physical layout of the connected vehicle system. (a) A connected automated vehicle (CAV) following a connected human-driven vehicle (CHV) along a road with the path coordinates s and s_1 highlighted. (b) Top view of the two vehicles with the direct distance d , the lateral distance d_{lat} and the course angle difference $\Delta\theta$ highlighted.

describe our experimental conditions and the vehicles participating in the experiments. The role of the latency, that occurs due to intermittent communication, state estimation, on-board computation, and actuation, will be explained in detail.

Fig. 2(a) shows a scenario where the brown connected human-driven vehicle (CHV) is followed by the white connected automated vehicle (CAV) along a road (of small curvature). The center points of the rear axles of the vehicles (marked R_1 and R) are used to describe the location of the cars; see the green and black trajectories. The corresponding path coordinates along the road are denoted by s_1 and s , while the velocities of the points are denoted by v_{R1} and v_R .

Both vehicles are equipped with GPS devices (mounted above the rear axle center points) and with V2X communication devices. Thus, the CAV can have access to the GPS position of point R_1 and the velocity v_{R1} (both its magnitude that is referred to as the speed as well as its direction that is called the heading angle); see Fig. 2(b). Comparing these with the GPS position of point R and the velocity v_R , the CAV can calculate the direct distance d , the lateral distance d_{lat} , and the course angle difference $\Delta\theta$ highlighted in Fig. 2(b). These quantities will be utilized when controlling the CAV's motion in order to follow the trajectory of the CHV. In particular, we will construct a longitudinal controller which uses the direct distance d and as well as the speeds of the vehicles ($|v_R|$ and $|v_{R1}|$), and construct a lateral controller that uses the lateral distance d_{lat} and the course angle difference $\Delta\theta$. For simplicity, we design the longitudinal and lateral controllers separately. However, we demonstrate that using these controllers simultaneously enables the CAV to follow the trajectory of the CHV while keeping a safe distance.

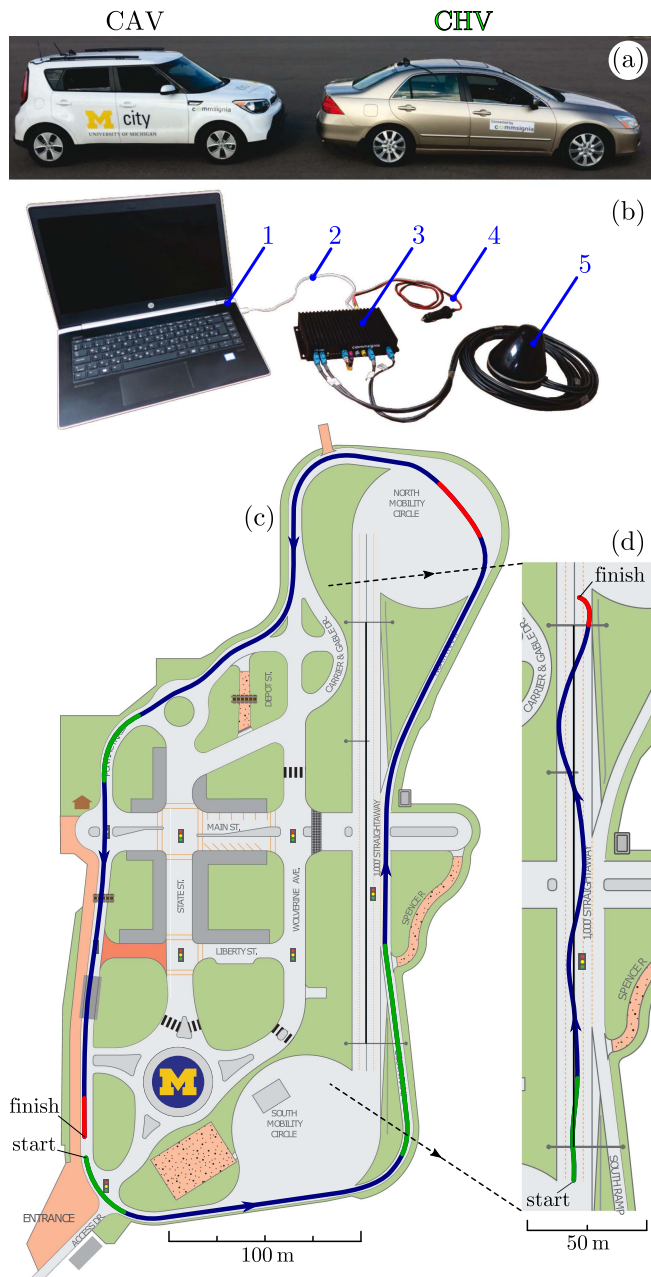


Fig. 3. Experimental setup. (a) Vehicles used in the experiments including the connected automated vehicle (CAV) and the connected human-driven vehicle (CHV). A GPS antenna is mounted above the center of the rear axle of each vehicle. (b) V2X communication device used in the experiments – 1: upper level computer, 2: ethernet cable, 3: electronic control unit, 4: power cable, 5: antennae. (c), (d) Mcity test track with representative trajectories followed during experiments. Routes are labeled with start, finish, and direction arrows. Along the blue segments of the trajectory steady state velocity was maintained, while green and red segments correspond acceleration and deceleration, respectively.

In order to prove the feasibility of V2X communication-based motion control, we experimentally validate the longitudinal and lateral controllers. We also demonstrate the performance of the CAV when the controllers are applied simultaneously. The vehicles, the V2X hardware, and the test environment are shown in Fig. 3. Both vehicles in panel (a) are equipped with commercial V2X communication devices which are shown in panel (b).

These allow us to collect GPS data from both vehicles. In case of the CAV, detailed vehicle data is also collected from the CAN bus and the on-board software allows us to control the throttle, the brakes, and the steering. Panels (c) and (d) show the Mcity test track highlighting some representative routes used when testing the longitudinal and lateral controllers, respectively. The color code indicates whether the vehicles accelerate (green), maintain steady speed (blue), or brake (red).

One significant difference of sensor-based and V2X communication-based control is how data collected, processed and used for control. When using on-board sensors, an automated vehicle typically collects data with high frequency and updates the control commands frequently (typically every 0.01-0.02 seconds). On the other hand, V2X data is only transmitted in every 0.1 seconds in order to maintain the bandwidth of the communication system for large number of connected vehicles [6]. This, together with the scheduling algorithms used for sending V2X packets and the computation time of the on-board computers, lead to 0.1-0.2 seconds delay between collecting the data at the CHV and utilizing this data in the control algorithms of the CAV. Moreover, GPS devices typically only take satellite data every 1 s and generate the data of 0.1 s resolution by applying state estimators (e.g., Kalman filters). Finally, the throttle, brake, and steering systems also contain actuation delays about 0.2-0.4 seconds. These effects together result in an effective latency of 0.6-1.0 seconds in the control loops. We will incorporate this delay in our control design and construct controllers that are robust against latency. Although the time delays in the control loops may vary in time, e.g., packet loss in the V2X communication can happen in a random fashion, we consider constant time delays for simplicity. Readers are referred to [16]–[18], where packet losses in connected cruise control and the time-varying delay in vehicle platooning are considered.

We will show experimentally that in spite of the significant delay and GPS errors the CAV is able to perform the required maneuvers when driving in a highway environment. In particular, it is able to follow the CHV's trajectory while keeping a safe distance. In the following sections, we provide the details of the longitudinal and lateral controllers before demonstrating the combined performance via connected lane change maneuvers.

III. LONGITUDINAL CONTROL DESIGN AND VALIDATION

The objective of the longitudinal controller is to enable the CAV to follow the CHV at a safe distance. Apart from avoiding collisions, we also require that the CAV attenuates the velocity disturbances of the CHV. To achieve these goals, the CAV will use the direct distance d , the speed of the CHV $|\mathbf{v}_{R1}|$ and its own speed $|\mathbf{v}_R|$; see Fig. 2(b). These goals are formulated mathematically and the designed controller is validated experimentally. We establish performance metrics for stability and disturbance attenuation that can be obtained by processing the experimental signals and allow us to fine tune the controller.

In order to simplify the modeling, one may notice that when the two vehicles are aligned, the speeds are well approximated by the derivatives of the path coordinates s and s_1 , i.e., $|\mathbf{v}_R| \approx \dot{s}$ and $|\mathbf{v}_{R1}| \approx \dot{s}_1$. Moreover, when the lateral distance between

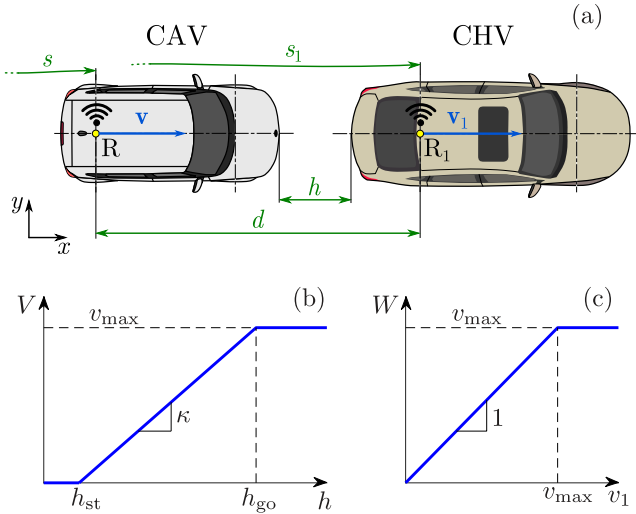


Fig. 4. Longitudinal car following. (a) Definitions of vehicle speed and space headway. (b) Range policy. (c) Speed policy.

the vehicles is small, one can approximate the direct distance as $d \approx s_1 - s$; see Fig. 4(a). When designing the controller, we will use the space headway defined as $h = d - l_e \approx s_1 - s - l_e$ where the effective vehicle length l_e is determined based on the geometry of the vehicles. Below, we use $l_e = 5$ m.

Based on these simplifications, the longitudinal control problem turns into the special connected cruise control (CCC) problem where the CAV utilizes information from the CHV immediately ahead [19], [20]. Here we build on these prior works, and we apply the longitudinal controller developed in [13], but we provide more details about the experimental evaluation of plant and string stability properties. In particular, we find the optimum control gains that provide the fastest decay of transients and establish performance indices that allow us to evaluate plant and string stability experimentally.

A. Vehicle Dynamics and Control Design

Neglecting drag, rolling resistance, road grade and drive train dynamics, the longitudinal motion of the CAV can be modeled by using the path coordinates and speed as

$$\begin{aligned} \dot{s} &= v, \\ \dot{v} &= \text{sat}(u(t - \tau_1)), \end{aligned} \quad (1)$$

where s denotes the longitudinal position and $v \approx |\mathbf{v}_R|$ denotes the speed of the connected automated vehicle, u is the commanded acceleration, and τ_1 represents the overall delay due to communication, computation, state estimation and actuation. We remark that, in case of the longitudinal dynamics, state estimation is typically accurate and the corresponding effective delay is negligible. On the other hand, the actuation delay can be significant, especially for vehicles with internal combustion engines, and this typically dominates τ_1 . For the CAV used in this paper, we experimentally identified $\tau_1 \approx 0.6$ s. The saturation function $\text{sat}(\cdot)$, wrapped around the commanded acceleration, corresponds to the physical limitations of the engine and the

brakes and saturates around -7 m/s² and 3 m/s² for our CAV according to the experiments.

The longitudinal controller commands the acceleration according to

$$u = \alpha(V(h) - v) + \beta(W(v_1) - v), \quad (2)$$

where α and β are feedback gains while the range policy $V(h)$ and the speed policy $W(v_1)$ are considered to be piece-wise linear functions where $v_1 \approx |\mathbf{v}_{R1}|$. The range policy shown in Fig. 4(b) is taken from [13] and it is given by

$$V(h) = \begin{cases} 0, & \text{if } h \leq h_{st}, \\ \kappa(h - h_{st}), & \text{if } h_{st} < h < h_{go}, \\ v_{max}, & \text{if } h \geq h_{go}, \end{cases} \quad (3)$$

where h_{st} is the headway distance below which the vehicle intends to stop, while above h_{go} the vehicle maintains the maximal speed v_{max} . Between these headway distances, the range policy is determined by the slope $\kappa = \frac{v_{max}}{h_{go} - h_{st}}$. In this paper, we will use $\kappa = 0.6$ 1/s which was chosen based on the comfort of the human occupants riding the CAV. The speed policy

$$W(v_1) = \begin{cases} v_1, & \text{if } v_1 \leq v_{max}, \\ v_{max}, & \text{if } v_1 > v_{max}, \end{cases} \quad (4)$$

is introduced to prohibit the CAV to follow a CHV that drives faster than v_{max} ; see Fig. 4(c).

In order to select the gain parameters α and β in the controller (2), we investigate how the CAV responds to the motion of the CHV in different scenarios. In particular, we study its transient and steady state responses in order to maximize safety and disturbance attenuation. The corresponding mathematical terms are referred to as plant stability and string stability [19] as explained further below.

To quantify plant and string stability, we linearize the closed loop system (1,2) about the constant speed motion. In case of small perturbations, the saturation function in (1) and the non-smooth characteristics of the range and speed policies in (2) can be omitted and the linearized system can be expressed as

$$\begin{aligned} \begin{bmatrix} \dot{\tilde{s}} \\ \dot{\tilde{v}} \end{bmatrix} &= \begin{bmatrix} 0 & 1 \\ 0 & 0 \end{bmatrix} \begin{bmatrix} \tilde{s} \\ \tilde{v} \end{bmatrix} + \begin{bmatrix} 0 & 0 \\ -\alpha\kappa & -(\alpha + \beta) \end{bmatrix} \begin{bmatrix} \tilde{s}(t - \tau_1) \\ \tilde{v}(t - \tau_1) \end{bmatrix} \\ &+ \begin{bmatrix} 0 & 0 \\ \alpha\kappa & \beta \end{bmatrix} \begin{bmatrix} \tilde{s}_1(t - \tau_1) \\ \tilde{v}_1(t - \tau_1) \end{bmatrix}, \end{aligned} \quad (5)$$

where the variables $\tilde{s} = s - v^*t$, $\tilde{v} = v - v^*$, $\tilde{s}_1 = s_1 - v^*t - h^* - l_e$, $\tilde{v}_1 = v_1 - v^*$ denote the perturbations about the equilibrium speed v^* ($0 < v^* < v_{max}$) and headway $h^* = V^{-1}(v^*)$. Using the speed perturbation of the CHV \tilde{v}_1 as input and the speed perturbation of the CAV \tilde{v} as output, we take the Laplace transform of (5) to derive the transfer function

$$H(\lambda) = \frac{\beta\lambda + \alpha\kappa}{\lambda^2 e^{\lambda\tau_1} + (\alpha + \beta)\lambda + \alpha\kappa}. \quad (6)$$

Plant stability (asymptotic stability of the equilibrium without external disturbance) can be investigated based on the characteristic function

$$D(\lambda) = \lambda^2 e^{\lambda\tau_1} + (\alpha + \beta)\lambda + \alpha\kappa, \quad (7)$$

that is given by the denominator of $H(\lambda)$. Here, we say the equilibrium is plant stable if and only if all the characteristic roots (obtained by solving the characteristic equation $D(\lambda) = 0$) have negative real parts, i.e., $\text{Re}\lambda_i < 0, i = 1, 2, \dots$. A stronger plant stability condition can be obtained by requiring that all roots have real parts smaller than δ , that is, $\text{Re}\lambda_i < \delta, i = 1, 2, \dots$

To find the corresponding boundaries in parameter space we substitute $\lambda = \delta + i\Omega$ into (7). When a real characteristic root is considered ($\Omega = 0$), we obtain a line in the plane of the control gains given by

$$\alpha = -\frac{\delta}{\delta + \kappa} (\beta + \delta e^{\delta\tau_1}). \quad (8)$$

In case of complex conjugate roots ($\Omega > 0$), one may obtain a curve in the form

$$\alpha = \frac{\delta^2 + \Omega^2}{\kappa\Omega} e^{\delta\tau_1} (\delta \sin(\Omega\tau_1) + \Omega \cos(\Omega\tau_1)),$$

$$\beta = -e^{\delta\tau_1} \left(\frac{\delta^2 - \Omega^2}{\Omega} \sin(\Omega\tau_1) + 2\delta \cos(\Omega\tau_1) \right) - \alpha, \quad (9)$$

which is parametrized by the frequency Ω . The plant stable domain is bounded by (8) and (9). As δ is decreased, the corresponding domain shrinks in the (α, β) plane as illustrated in Fig. 5(a) for $\kappa = 0.6$ 1/s (corresponding to $h_{st} = 5$ m, $h_{go} = 55$ m, $v_{max} = 30$ m/s in accordance with the setup used in [13]) and $\tau_1 = 0.6$ s (that was identified experimentally to our CAV).

Having gain parameters that ensure plant stability for smaller real parts is considered to be beneficial for safety as it allows transients to decay faster. The optimal scenario corresponds to the minimal value of δ as this makes the transients decay most rapidly. Based on the topology of the curves given by (8) and (9) the minimum real part of the rightmost root can be calculated analytically:

$$\delta_{min} = \frac{\sqrt{2} - 2}{\tau_1}. \quad (10)$$

This corresponds to the optimal control gains

$$\alpha_{opt} = \frac{10\sqrt{2} - 14}{\kappa\tau_1^2} e^{\sqrt{2}-2} \approx \frac{0.0791}{\kappa\tau_1^2},$$

$$\beta_{opt} = \frac{2\sqrt{2} - 2}{\tau_1} e^{\sqrt{2}-2} - \alpha_{opt} \approx \frac{0.4611}{\tau_1} - \alpha_{opt}, \quad (11)$$

which are marked by the green square in Fig. 5(a). We remark that selecting the control gains as above may not formally guarantee collision avoidance. Such guarantees need to take into account the acceleration limits of the CHV and the CAV; cf. the saturation in (1). Then one may utilize barrier functions [21], [22] or formal verification [23] to ensure safety.

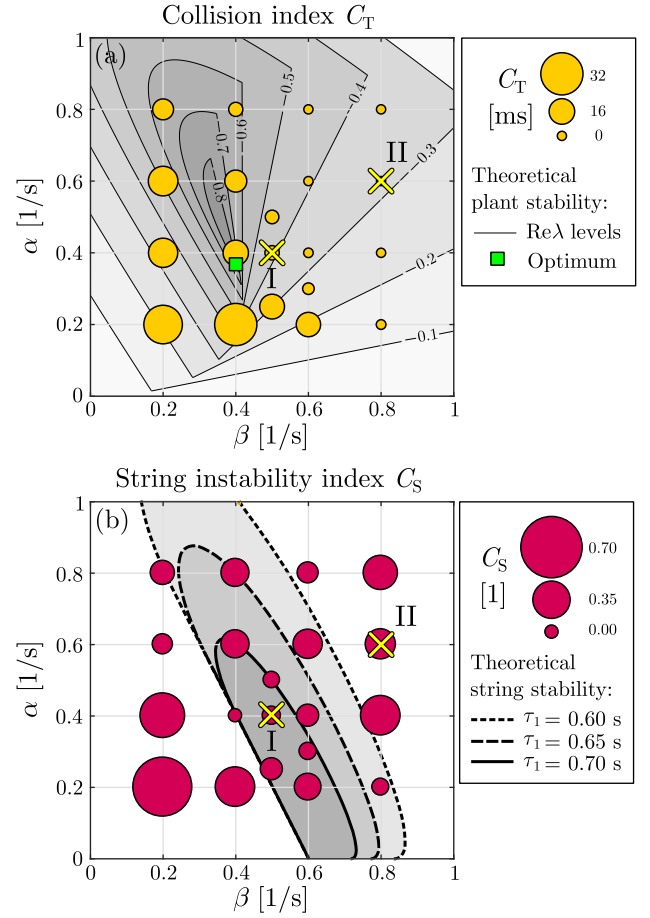


Fig. 5. Stability charts in the (β, α) plane illustrating plant stability (a) and string stability (b). In panel (a), the black curves bound the stable domains for different values of the real part of the rightmost characteristic roots (as indicated) for $\kappa = 0.6$ 1/s and $\tau_1 = 0.6$ s. The green square marks the optimal control gains with respect to plant stability. The yellow dots correspond to the collision index obtained experimentally for different gain combinations: larger dots represent larger index values. In panel (b), the black curves bound the string stable domain for $\kappa = 0.6$ 1/s and $\tau_1 = 0.6, 0.65, 0.7$ s. The red dots correspond to the string instability index obtained via experiments: again larger dots represent larger index values. The gain combinations marked I and II correspond to the experimental runs in Fig. 6.

String stability (attenuation of speed fluctuations of the leading car by the following car, see also [24]–[26]) can also be determined by using the transfer function (6). Namely, the system is declared string stable if the magnitude of the transfer function is below 1 for any harmonic excitation, i.e., $|H(i\omega)| < 1, \forall \omega > 0$; see [19], [20]. Again, our goal is to turn this condition to a stability chart on the plane of feedback gains α and β . As shown in [20], the string stability loss at $\omega = 0$ is given by $|H''(0)| = 0$ since $|H(0)| = 1$ and $|H'(0)| = 0$ for all parameter combinations. This results in the lines

$$\alpha = 0, \quad \alpha = 2(\kappa - \beta). \quad (12)$$

When the string stability loss occurs for $\omega = \hat{\omega} > 0$, the string stability conditions are given by $|H(i\hat{\omega})| = 1, |H'(i\hat{\omega})| = 0$.

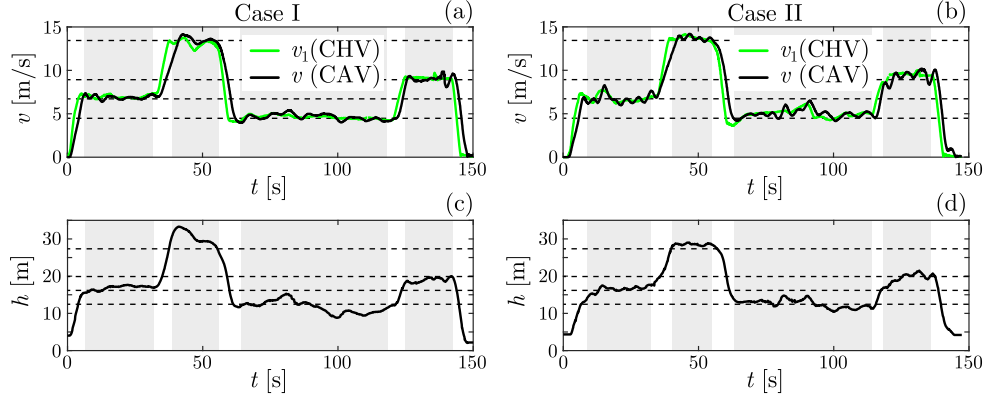


Fig. 6. Data collected for longitudinal car-following. Case I: $\alpha = 0.4$ 1/s and $\beta = 0.5$ 1/s; Case II: $\alpha = 0.6$ 1/s and $\beta = 0.8$ 1/s. The time segments where the leading vehicle (CHV) is trying to maintain a constant velocity and the following vehicle (CAV) settles close to steady state are shaded in grey. Panels (a) and (b) show the velocities of the CHV and the CAV. The intended steady state speed values v^* are marked by dashed lines. The headway of the CAV is shown in panels (c) and (d); dashed lines highlight the steady state values $h^* = V^{-1}(v^*)$.

These result in the curves

$$\alpha = a \pm \sqrt{a^2 + b},$$

$$\beta = \frac{\hat{\omega} + \alpha \kappa \tau_1 \sin(\hat{\omega} \tau_1)}{\sin(\hat{\omega} \tau_1) + \hat{\omega} \tau_1 \cos(\hat{\omega} \tau_1)} - \alpha, \quad (13)$$

with

$$a = \frac{\hat{\omega}(\kappa \tau_1 - 1) + \kappa \sin(\hat{\omega} \tau_1) \cos(\hat{\omega} \tau_1)}{(2\kappa \tau_1 - 1) \sin(\hat{\omega} \tau_1) - \hat{\omega} \tau_1 \sin(\hat{\omega} \tau_1)},$$

$$b = \frac{\hat{\omega}^2 (\sin(\hat{\omega} \tau_1) - \hat{\omega} \tau_1 \cos(\hat{\omega} \tau_1))}{(2\kappa \tau_1 - 1) \sin(\hat{\omega} \tau_1) - \hat{\omega} \tau_1 \sin(\hat{\omega} \tau_1)}, \quad (14)$$

which are parametrized by the angular frequency $\hat{\omega}$. The string stable domain is bounded by (12) and (13) as shown in Fig. 5(b) for $\kappa = 0.6$ 1/s and three different delays values $\tau_1 = 0.6, 0.65, 0.7$ s. Notice that the string stable domain shrinks as the delay is increased, and it disappears for $\tau_1 > 1/(2\kappa)$; see [20]. Selecting feedback gains that are included in the string stable domains for larger delays would allow the CAV to attenuate the velocity fluctuations of the CHV in a robust manner; see [27].

B. Experimental Validation

In order to validate the theoretical design and tune the feedback gains, we carried out a set of experiments with the vehicles described in Section II. In these experiments, the CAV followed the CHV along the route shown in Fig. 3(c) according to a specific speed profile. Namely, the human driver of the leading vehicle performed a driving cycle where steady state speed was maintained over four separate time intervals (blue segments in Fig. 3(c)) and these sections were connected by accelerating the decelerating maneuvers (green and red segments in Fig. 3(c)). During the experiments, the connected automated vehicle used the controller (2) to govern its longitudinal motion whilst being steered by a human operator. For each lap we set a certain gain pair α and β , and collected the GPS positions and velocities of the two vehicles throughout the test.

Experimental results for two different gain setups (Case I and Case II) are shown in Fig. 6. The speed and the headway

profiles are plotted in panels (a)-(b) and (c)-(d), respectively. As depicted by the green curves in Fig. 6(a,b), first, the CHV accelerates from a stop to 15 mi/hr and holds it in the first steady speed section (shaded gray). In the second, third, and fourth steady speed sections, it keeps its speed at 30, 10 and 20 mi/hr, respectively. At the end of the lap, the vehicles come to a halt. Observe that the evolution of the speed and headway of the CAV clearly depends on the applied control gains. In particular, the time signals of Case I are smoother; signals of Case II exhibit undesired vibrations.

In order to select the gains that provide the best longitudinal performance for the CAV, we use two criteria. To maintain safety, we want the CAV to be able drop its speed fast enough when the CHV is dropping its speed. Hence, our first measure of longitudinal performance uses the instantaneous time-to-collision

$$T(t) = \frac{h(t)}{v(t) - v_1(t)}, \quad (15)$$

which is the time needed to avoid collision if the speeds of the vehicles were kept constant. We define the collision index

$$C_T(\alpha, \beta) = \frac{1}{t_{\text{end}} - t_{\text{ini}}} \int_{t_{\text{ini}}}^{t_{\text{end}}} \text{ReLu}(T_c - T(t)) dt, \quad (16)$$

where $\text{ReLu}(x) = \max\{0, x\}$ and t_{ini} and t_{end} represent the start and end times of the run. Also, T_c denotes a threshold for time to collision below which we consider the car following to be unsafe. For our purposes, we set $T_c = 2$ s. Larger values of C_T indicate that the following connected automated vehicle gets closer to colliding with the connected human-driven vehicle ahead, and thus, constitutes an undesirable design.

We also desire that the CAV attenuates the velocity perturbations that is beneficial for fuel economy [28] and congestion avoidance [29]. Thus, the second performance measure aims to evaluate string stability. Here we define the string instability index

$$C_s(\alpha, \beta) = \frac{1}{f_{\text{end}} - f_0} \int_{f_0}^{f_{\text{end}}} \text{ReLu}\left(\frac{G(f)}{G_1(f)} - 1\right) df, \quad (17)$$

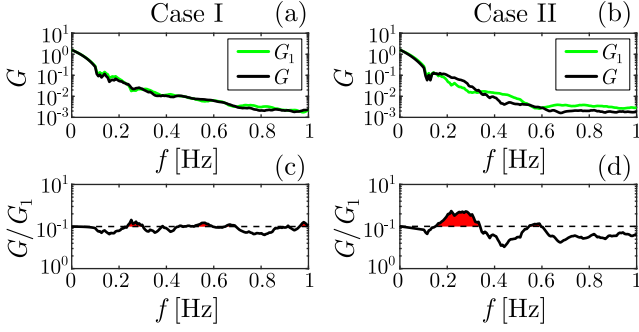


Fig. 7. Frequency analysis of the velocities of the experimental runs shown in Figs. 6. Case I: $\alpha = 0.4$ 1/s and $\beta = 0.5$ 1/s; Case II: $\alpha = 0.6$ 1/s and $\beta = 0.8$ 1/s. (a)-(b) The Fourier transforms of the velocities of the CHV (green) and CAV (black). (c)-(d) The corresponding Fourier transform ratios with the area above 1 highlighted as red.

where $G_1(f)$ and $G(f)$ represent the magnitudes of the Fourier transforms of the speed signals of the CHV and the CAV, respectively. The limits of the integration $f_0 = 0$ Hz and $f_{\text{end}} = 1$ Hz cover the relevant frequency range that is characteristic for the velocity fluctuations in our experiments. Larger values of the string instability index C_s indicate that velocity fluctuations coming from the CHV tend to get amplified by the CAV, which is not desirable.

Fig. 7(a) and (b) shows the magnitudes of the Fourier transforms for Cases I and II, respectively, for the velocity signals given in Fig. 6(a) and (b). Note that we performed the Fast Fourier transforms and filtered the results using the Savitzky-Golay filter with a 3rd order polynomial and frame length of 31 points. The ratio of these functions are depicted in panels (c) and (d) for Cases I and II, respectively. As highlighted by red shading, the velocity fluctuations are amplified more significantly in Case II than in Case I.

The indices (16) and (17) are computed for all experimental runs (with 21 different control gain setups) and the results are visualized by the colored dots in the (β, α) plane in Fig. 5. Larger index values correspond to larger dots. Note that small values are desirable for both indices. The previously presented experimental runs noted by Case I and Case II are also marked in the figure. In panel (a), the collision index is compared to the plant stability contours (given by (8) and (9)). One may notice the correlation between the dots of different sizes and the contours suggesting that low gains are not desirable for safety considerations. In panel (b), the string instability index is compared to the theoretical string stability boundaries. In this case, there is strong correlation between the shape of the theoretically string stable domains and the dots of different sizes, suggesting that one should avoid both the high as well as the low gain domains.

Based on the results shown in Fig. 5, we chose $\alpha = 0.4$ 1/s and $\beta = 0.5$ 1/s as a final gain set (related to Case I). This setup yielded low values for both the collision and the string instability indices. Moreover, it is also located close to the optimal control gain setup of plant stability, and it is inside the analytical string stability boundaries for the delays examined.

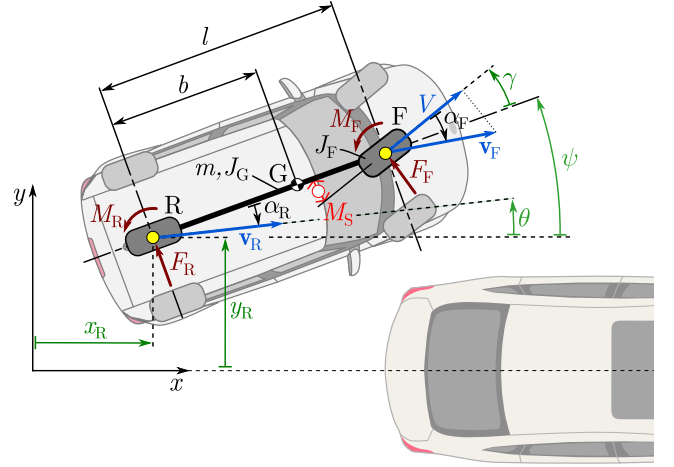


Fig. 8. Lateral path following where the CAV aims to follow the x -axis – the path of a hypothetical leading vehicle.

IV. LATERAL CONTROL DESIGN AND VALIDATION

The objective of the lateral controller is to enable the CAV to follow the trajectory of the CHV with little lateral deviation d_{lat} and course angle difference $\Delta\theta$; see Fig. 2(b). Note that, for each vehicle, the course angle is defined as the angle between the velocity of the center of the rear axle (where the GPS is mounted) and the x axis. In order to simplify the control design, we assume that the leading vehicle (CHV) moves along the x axis, that is, it has zero course angle and zero lateral displacement; see Fig. 8. In this case, the course angle difference is given by the course angle of the following vehicle (CAV): $\Delta\theta = \theta$, while the lateral distance is given by the lateral position of the CAV: $d_{\text{lat}} = y_R$. Indeed, such assumptions are valid in scenarios when the CHV is moving along a path of small curvatures that are typical in highway-driving scenarios. For roads with higher curvature more sophisticated controllers may be considered [30]–[37]. Below, we formulate the path following problem mathematically and validate the designed controller while utilizing a performance measure for stability. Again, this measure is obtained by processing the experimental signals and used to fine tune the controller.

A. Vehicle Dynamics and Control Design

To describe the lateral and yaw motion of the CAV, we utilize an in-plane, single-track model with front wheel drive as depicted in Fig. 8. The mass and the mass moment of inertia with respect to the center of gravity G are denoted by m and J_G , respectively. The wheelbase (i.e., the distance between the axle center points R and F) is l while the distance between the rear axle center point R and center of mass G is b . The overall mass moment of inertia of the steering system is J_F . The front wheel of the vehicle is steered via the steering torque M_S that acts as an internal torque between the front wheel and the chassis. The lateral forces and self-aligning moments of the front and rear tires are denoted by F_F , F_R , M_F and M_R , respectively.

To derive the equations of motion, the Appell-Gibbs formalism can be used; see [38], [39]. This requires the introduction

of the so-called pseudo velocities. Since the configuration is described by four generalized coordinates (i.e., the coordinates x_R and y_R of point R, the yaw angle ψ and the steering angle γ) and there is one nonholonomic constraint (the longitudinal velocity V of the front wheel is kept constant), we need to choose three pseudo-velocities; see Appendix A. Here, we choose σ (the lateral velocity of point R), ω (the yaw rate of the vehicle), and Ω (the steering rate, i.e., the yaw rate of front axle relative to the car). Thus, the velocity state of the vehicle can be described by

$$\begin{aligned} \dot{x}_R &= V \frac{\cos \psi}{\cos \gamma} - \sigma \frac{\sin(\psi + \gamma)}{\cos \gamma} - l\omega \cos \psi \tan \gamma, \\ \dot{y}_R &= V \frac{\sin \psi}{\cos \gamma} + \sigma \frac{\cos(\psi + \gamma)}{\cos \gamma} - l\omega \sin \psi \tan \gamma, \\ \dot{\psi} &= \omega, \\ \dot{\gamma} &= \Omega. \end{aligned} \quad (18)$$

These equations give part of the governing equations, while the other part is comprised of the Appell-Gibbs equations (see details in Appendix A):

$$\begin{bmatrix} m_{11} & m_{12} & 0 \\ m_{21} & m_{22} & J_F \\ 0 & J_F & J_F \end{bmatrix} \begin{bmatrix} \dot{\sigma} \\ \dot{\omega} \\ \dot{\Omega} \end{bmatrix} = \begin{bmatrix} f_1 \\ f_2 \\ f_3(M_S) \end{bmatrix}, \quad (19)$$

where the elements of the generalized mass matrix are given by

$$\begin{aligned} m_{11} &= \frac{m}{\cos^2 \gamma}, \\ m_{12} &= m_{21} = m(b + l \tan^2 \gamma), \\ m_{22} &= J_G + J_F + m(b^2 + l^2 \tan^2 \gamma), \end{aligned} \quad (20)$$

while the right hand side can be expressed as

$$\begin{aligned} f_1 &= \frac{F_F}{\cos \gamma} + F_R - \frac{m}{\cos \gamma} (V - (l - b)\omega \sin \gamma) \omega \\ &\quad + \frac{m \sin \gamma}{\cos^3 \gamma} (V \sin \gamma - \sigma - l\omega) \Omega, \\ f_2 &= \frac{F_F l}{\cos \gamma} - \frac{m}{\cos \gamma} (bV + (l - b)\sigma \sin \gamma) \omega \\ &\quad + \frac{ml \sin \gamma}{\cos^3 \gamma} (V \sin \gamma - \sigma - l\omega) \Omega + M_F + M_R, \\ f_3 &= M_F + M_S. \end{aligned} \quad (21)$$

The tire forces $F_F(\alpha_F)$, $F_R(\alpha_R)$ and self-aligning moments $M_F(\alpha_F)$, $M_R(\alpha_R)$ are calculated via the brush tire model given in Appendix B. The side slip angles α_F and α_R of the front and rear tires can be determined based on vehicle kinematics as

$$\begin{aligned} \tan \alpha_F &= -\frac{\sigma + l\omega}{V \cos \gamma} + \tan \gamma, \\ \tan \alpha_R &= \frac{\sigma \cos \gamma}{-V + (\sigma + l\omega) \sin \gamma}, \end{aligned} \quad (22)$$

respectively.

We construct a hierarchical controller to regulate the steering torque M_S in order to make the CAV to perform path following.

In particular, it aims to follow the x -axis, that is, to reduce both the course angle θ and the lateral position y_R to zero; see Fig. 8. At the higher-level, we set the desired steering angle

$$\gamma_{\text{des}} = -k_y y_R - k_\theta \sin \theta, \quad (23)$$

where the course angle can be expressed by the yaw angle and the rear slip angle as $\theta = \psi - \alpha_R$, while k_θ and k_y are the control gains. Then, the steering torque is determined by the lower-level PID controller

$$M_S = k_p(\gamma_{\text{des}}(t - \tau_2) - \gamma) + k_d(\dot{\gamma}_{\text{des}}(t - \tau_2) - \dot{\gamma}) + k_i z, \quad (24)$$

where

$$\dot{z} = \gamma_{\text{des}}(t - \tau_2) - \gamma, \quad (25)$$

and k_p , k_d and k_i are the proportional, derivative and integral control gains of the lower-level controller, respectively. We remark that one may construct more complicated controllers; see, for instance, those in [40].

Moreover, τ_2 represents the time delay arising from communication, computation, state estimation, and actuation. In case of the lateral motion, a significant part of the delay arises from the state estimation while the actuation delay is typically much smaller compared to the longitudinal case. The impact of the time delays corresponding to the different levels of the steering control was analyzed in [41]. It was shown that the time delay of the lower-level controller has to be below a small critical value (≈ 1 ms), but if this condition is satisfied, the time delay of the higher-level controller plays the key role in determining the stability of the lateral motion control. For our CAV, we experimentally identified $\tau_2 \approx 0.8$ s.

The closed-loop dynamics of the vehicle is described by (18,19,23,24,25) that can be written into the form of a delay differential equation of a neutral type:

$$\dot{\mathbf{x}}(t) = \phi(\mathbf{x}(t), \mathbf{x}(t - \tau_2), \dot{\mathbf{x}}(t - \tau_2)), \quad (26)$$

where

$$\mathbf{x} = [\sigma \ \omega \ \Omega \ x_R \ y_R \ \psi \ \gamma \ z]^T, \quad (27)$$

contains the state variables. When the vehicle moves along the x -axis at a constant speed V , the motion is given by

$$\mathbf{x}^* = \begin{bmatrix} 0 & 0 & 0 & Vt & 0 & 0 & 0 & 0 \end{bmatrix}^T. \quad (28)$$

Let us introduce the perturbations $\tilde{\mathbf{x}} = \mathbf{x} - \mathbf{x}^*$ and linearize (26) about the straight-line motion to obtain

$$\dot{\tilde{\mathbf{x}}}(t) = \mathbf{M}^{-1}(\mathbf{A}_0 \tilde{\mathbf{x}}(t) + \mathbf{A}_\tau \tilde{\mathbf{x}}(t - \tau_2) + \mathbf{B}_\tau \dot{\tilde{\mathbf{x}}}(t - \tau_2)), \quad (29)$$

where the matrices \mathbf{M} , \mathbf{A}_0 , \mathbf{A}_τ and \mathbf{B}_τ are given in Appendix C.

Using an exponential trial solution, we can obtain the characteristic function

$$D(\lambda) := \det(-\lambda \mathbf{M} + \mathbf{A}_0 + \mathbf{A}_\tau e^{-\lambda \tau_2} + \lambda \mathbf{B}_\tau e^{-\lambda \tau_2}). \quad (30)$$

The characteristic equation $D(\lambda) = 0$ has infinitely many solutions for the characteristic roots λ . Notice that $\lambda = 0$ is always a solution corresponding to the ‘neutral’ direction x . Thus, we introduce $\tilde{D}(\lambda) = D(\lambda)/\lambda$, by which, $\tilde{D}(0) = 0$ provides the stability boundaries for non-oscillatory stability loss whereas

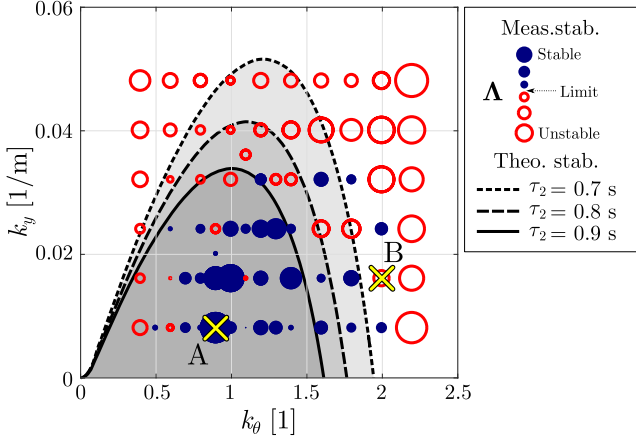


Fig. 9. Stability charts in the (k_θ, k_y) plane. Black curves represent the theoretical stability boundaries for $\tau_2 = 0.7, 0.8, 0.9$ s. Red circles and blue dots correspond to the experimentally identified unstable and stable control gain pairs, respectively. The larger the circle/dot is, the more unstable/stable the system is. For the parameter pairs marked by A and B, measured and simulated trajectories of the vehicle are compared in Fig. 10.

TABLE I
VEHICLE, TIRE AND LOWER-LEVEL CONTROLLER PARAMETERS

Parameter name	Value	Unit
l	2.57	m
b	1.54	m
m	1770	kg
J_G	1343	kgm ²
J_F	0.25	kgm ²
V	15	m/s
a	0.1	m
k	2×10^6	N/m ²
μ_0	0.9	-
μ	0.6	-
k_p	640	Nm
k_d	8	Nms
k_i	40	Nm/s

$\tilde{D}(i\Omega) = 0$ gives the stability boundaries for oscillatory stability loss; see [42]. These curves bound the stable domain in the parameter space where all characteristic roots have negative real part.

Due to the complexity of the characteristic (30) we calculate the stability boundaries numerically using semi-discretisation; see [43]. In particular, we utilize Chebyshev polynomials and the Chebyshev differentiation matrix to approximate the spectrum; see [44]. The results are summarized in Fig. 9 as stability charts in the plane of the higher-level control gains k_θ and k_y for different values of the delay $\tau_2 = 0.7, 0.8, 0.9$ s. The remaining parameters and the lower level control gains are given in Table I. The black curves represent the stability boundaries and one may notice that the shaded stable domain shrinks as the time delay is increased. The effects of the longitudinal velocity and time delay on the linear stability are investigated theoretically in Appendix D.

B. Experimental Validation

We carried out experiments with the connected automated vehicle for different higher-level gain combinations using the straight multi-lane segment of the Mcity test track; see Fig. 3(d). In the test runs, the CAV aimed to follow the straight lane center-line given by GPS coordinates. The time histories of the longitudinal and lateral positions, the course angle, and the steering angle were recorded; cf. (27). Fig. 11 shows our connected automated vehicle during one of these lateral control experiments where the trajectory of the vehicle is plotted as a black curve. Increasing lateral oscillations can be observed corresponding to the choice of control gains in this particular test.

To characterize the lateral stability, we analysed the lateral oscillations of the vehicle using the recorded signals. Since oscillations were observed for all the control gain setups, we utilized the concept called logarithmic decrement

$$\Lambda := \frac{1}{2} \ln \frac{A_0}{A_1}. \quad (31)$$

The peak-to-peak oscillation amplitudes A_i , marked in Fig. 10, allow us to obtain information about the real part of the right-most complex conjugate characteristic roots of (30). In particular, having rightmost roots with negative/positive real parts corresponds to linearly stable/unstable lane keeping with decreasing/increasing vibration amplitudes. Fig. 9 summarizes the experimental results in the plane of the higher-level control gains k_θ and k_y . Blue dots and red circles refer to linearly stable and unstable behavior, respectively. The larger the dots/circles are, the more stable/unstable the lane keeping control is. For each of the 60 different control gain setups shown in the figure, experimental runs were carried out three times. Generally, measurement noise makes the system more unstable. Thus, for each control gain setup, the largest logarithmic decrement was chosen from the three identified values, supposing that this is the closest value to the noise-free case. The experimental results show good agreement with the theoretical stability chart validating the necessity of taking into account the time delays in the control design.

The measurement results were also compared to numerical simulations in Fig. 10 in order to validate the model constructed above. For the gain combinations marked A and B in Fig. 9 we compare the recorded trajectories with those obtained by simulating the nonlinear model (18,19,23,24,25). The parameters listed in Table I were used considering $\tau_2 = 0.8$ s. Note that rather than setting the longitudinal velocity to $V = 15$ m/s, we used the speed data recorded during the experiments as shown in Fig. 10(a,b). The corresponding lateral positions are plotted in Fig. 10(c,d). The simulation results are shown by thick dashed curves while the measured signals are plotted by thin solid lines. Cases A and B correspond to stable and unstable control gain setups, respectively. In terms of stability, there is a good agreement between the simulations and the experimental results and the oscillation frequencies are also very close in the unstable case B. There are some mismatches in terms of amplitudes which is primarily due to the inaccuracy of satellite navigation

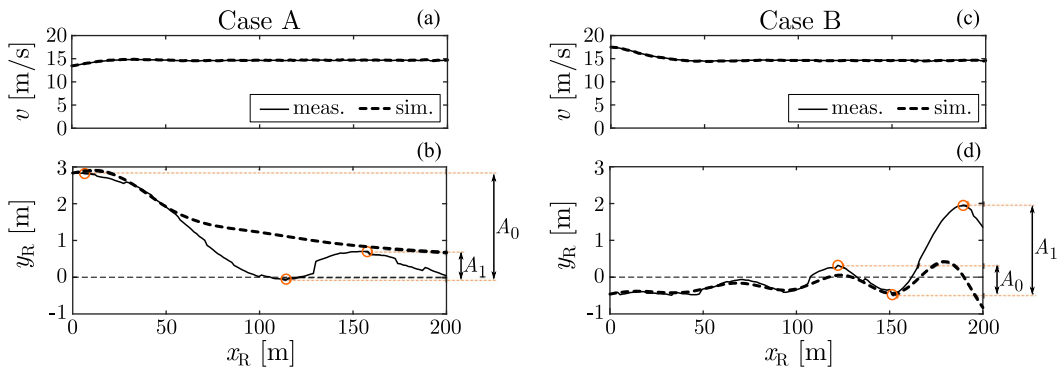


Fig. 10. Measured (thin solid line) and simulated (thick dashed line) trajectories of the CAV for stable (A) and unstable (B) control gain combinations in Fig. 9. Thin dashed line illustrates the desired rectilinear motion. In the simulations $\tau_2 = 0.8$ s was considered. Panels (a) and (b) show the speed while panels (c) and (d) depict the lateral positions of the CAV along the track. The peak-to-peak amplitudes, used for calculating the logarithmic decrement are also marked as the vertical distances between orange circles.

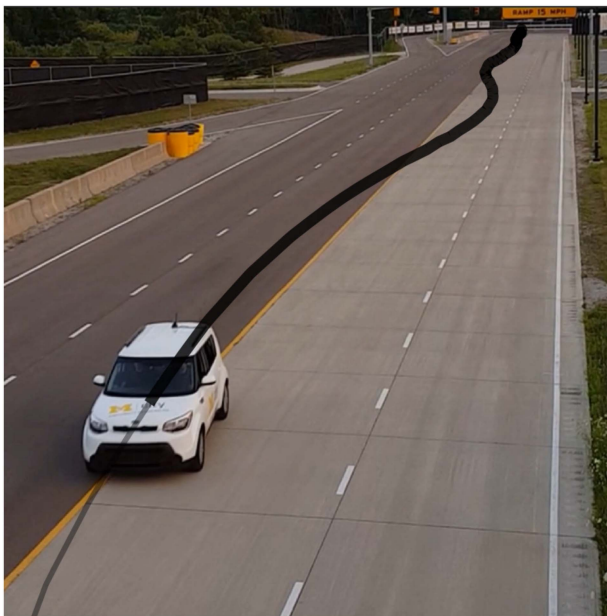


Fig. 11. Picture from one of the lateral control experiments with the trajectory of the CAV highlighted by a black curve.

(appr. 0.7 m) and infrequent corrections of the state estimators (every 1 s) embedded in the GPS units. The simulation results show that the time delay plays an important role in the stability; omitting the delay would result in stable motion for both control gain setups.

Still, despite the inaccuracy and delay in GPS sensing and estimation, careful tuning of the lateral controllers enabled the CAV to follow the desired path. A similar statement also holds for the longitudinal controller designed in the previous section. In what follows, we integrate the lateral and longitudinal controllers and test their combined performance when the CAV aims to follow the path of the CHV while keeping a safe distance.

V. CONNECTED LANE CHANGE EXPERIMENTS

After designing and experimentally validating the longitudinal and lateral controllers of the connected automated vehicle,

we deploy these controllers simultaneously. Based on the general setup laid out in Fig. 2, the control laws given by (2) and (23) can be generalized to

$$u = \alpha (V(d - l_e) - v) + \beta (W(v_1) - v), \quad (32)$$

and

$$\gamma_{\text{des}} = -k_y d_{\text{lat}} - k_\theta \sin \Delta\theta, \quad (33)$$

respectively. We apply these in a scenario where the leader (CHV) makes lane changes and the CAV follows the same path while keeping a safe distance; see the green and black trajectories in Fig. 13(d).

In order to test the robustness of the control strategy, the CAV was deployed to follow the CHV using different initial conditions before executing the lane changes. The longitudinal speeds of the cars were similar but the headway was varied in the different runs. Specifically, the initial speed of both vehicles were close to 15 m/s, while the initial headway of the CAV was initialized to be equal, larger or smaller than the desired headway ($h_{\text{des}} = V^{-1}(v_1)$) given by the range policy (3) depicted in Fig. 4(b).

The corresponding experimental results are shown in Fig. 12. Case N (panels (a)-(c)) shows a lane change where the initial headway was approximately equal to the desired one. Panel (a) depicts the positions of the CHV (green circles) and the CAV (black dots) along the track. The size of the circles and dots are proportional to the speed of the vehicles. Panel (b) shows the speed of the vehicles applying the same color code, while panel (c) compares the desired headway (dashed curve) with actual headway (solid curve). As shown by these examples, the longitudinal controller maintains the desired headway and also damps the speed fluctuation of the CHV, while the lateral controller reduces the lateral distance between the trajectories of the CAV and CHV. At the end of the test, both cars stop while a safe headway is maintained. Case L (panels (d)-(f)) corresponds to a larger headway initialization. Notice that while the CAV follows the CHV to the next lane it also “catches up” by reducing the headway to the desired value, demonstrating the simultaneous operation of the lateral and longitudinal controllers. Case S (panels (g)-(i)) depicts a lane change with smaller headway

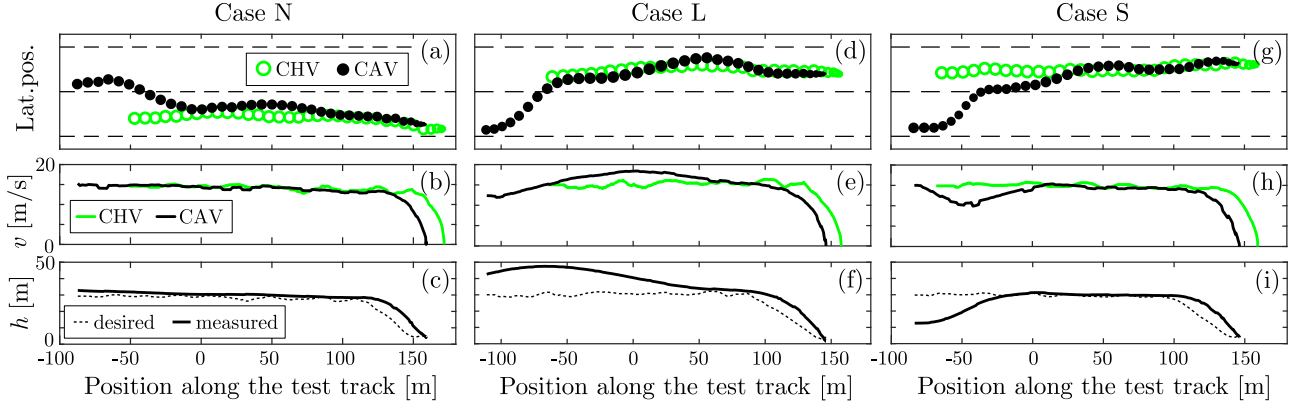


Fig. 12. Connected lane change experiments where the CAV follows the CHV. Cases N, L and S show lane change scenarios with different initial headways. The positions of the CHV (green circles) and the CAV (black dots) are shown in panel (a), (d) and (g) along the test track. Sizes of the marks are proportional to the vehicle’s speed. Panels (b), (e) and (h) shows the speed of the vehicles, while panels (c), (f) and (i) depict the desired headway (thin dashed line) and the measured headway (thick solid line) of the CAV.

initialization. Here the CAV “drops back” by increasing the headway while executing the lane change at the same time.

Finally, Case DL in Fig. 13 depicts a double lane change with smaller initial headway. Again, the CAV corrects the headway to achieve the desired value while imitating the lane changes of the CHV from one lane to the other and back. A picture about the experiment is also shown in panel (d) with the trajectories of the CHV (green) and the CAV (black).

VI. CONCLUSION

The concept of connectivity-based vehicle control has been put forward in this paper to demonstrate how automated vehicles can retain their automated functionalities when their optical sensors are compromised. In particular, we designed lateral and longitudinal controllers for a connected automated vehicle (CAV) to respond to the motion of a connected human-driven vehicle (CHV) based on information received via vehicle-to-everything (V2X) connectivity. By taking into account the latencies in the control design, we were able to achieve lateral and longitudinal stability for the motion of the CAV corresponding to tracking the CHV. We tested the controllers experimentally and validated the stability charts by introducing performance metrics that enable the comparison of different controller parameters based on the recorded time signals. The results allowed us to select the control gains that ensure robustness against time delays. The longitudinal and lateral controllers were deployed simultaneously allowing the CAV to follow the CHV while changing lanes, achieving similar behavior to a human driver in limited visibility conditions when sensory data is limited. In the future, we will consider using V2X to allow the connected automated vehicle to perform more complex maneuvers based on information coming from connected vehicles and connected infrastructure.

APPENDIX A

DERIVATION OF THE EQUATIONS OF MOTION OF THE SINGLE-TRACK MODEL WITH THE APPELL-GIBBS METHOD

In case of front wheel drive, the assumption of the constant longitudinal velocity V of the front wheel (i.e., the velocity

component parallel to the wheel plane) can be given by the kinematic constraint:

$$\dot{x}_R \cos(\psi + \gamma) + \dot{y}_R \sin(\psi + \gamma) + l\dot{\psi} \sin \gamma = V, \quad (34)$$

which reduces the dimension of the velocity state by one. In order to eliminate the constraint (34), one can replace the four generalised velocities $\dot{x}_R, \dot{y}_R, \dot{\psi}, \dot{\gamma}$ with three pseudo velocities that can be chosen intuitively. We use the lateral velocity of the rear wheel, the yaw rate, and the steering rate, that is,

$$\begin{aligned} \sigma &:= -\dot{x}_R \sin \psi + \dot{y}_R \cos \psi, \\ \omega &:= \dot{\psi}, \\ \Omega &:= \dot{\gamma}, \end{aligned} \quad (35)$$

respectively. The kinematic constraint (34) and the definition of the pseudo velocities (35) compose a system of linear algebraic equations with respect to the generalized velocities. Solving this equation, the generalized velocities can be expressed as functions of the pseudo velocities; see (18). These expressions provide one part of the governing equations since they define the relationship between the configuration space and the velocity space.

The remaining equations, needed to describe the motion of the vehicle, can be determined by the Appell-Gibbs method, which is based on the use of the so-called acceleration energy. For our model it can be calculated as

$$\mathcal{A} = \frac{1}{2} m a_G^2 + \frac{1}{2} J_G \omega^2 + \frac{1}{2} J_F (\dot{\omega} + \dot{\Omega})^2 + \dots, \quad (36)$$

where a_G is the acceleration of the center of mass G. After some algebraic manipulation the acceleration energy reads:

$$\begin{aligned} \mathcal{A} &= \frac{1}{2} \frac{m}{\cos^2 \gamma} \dot{\sigma}^2 + \frac{1}{2} (J_G + J_F + m (b^2 + l^2 \tan^2 \gamma)) \dot{\omega}^2 \\ &\quad + \frac{1}{2} J_F \dot{\Omega}^2 + m (b + l \tan^2 \gamma) \dot{\sigma} \dot{\omega} + J_F \dot{\omega} \dot{\Omega} \\ &\quad + \frac{m}{\cos \gamma} (V - (l - b) \omega \sin \gamma) \omega \dot{\sigma} \end{aligned}$$

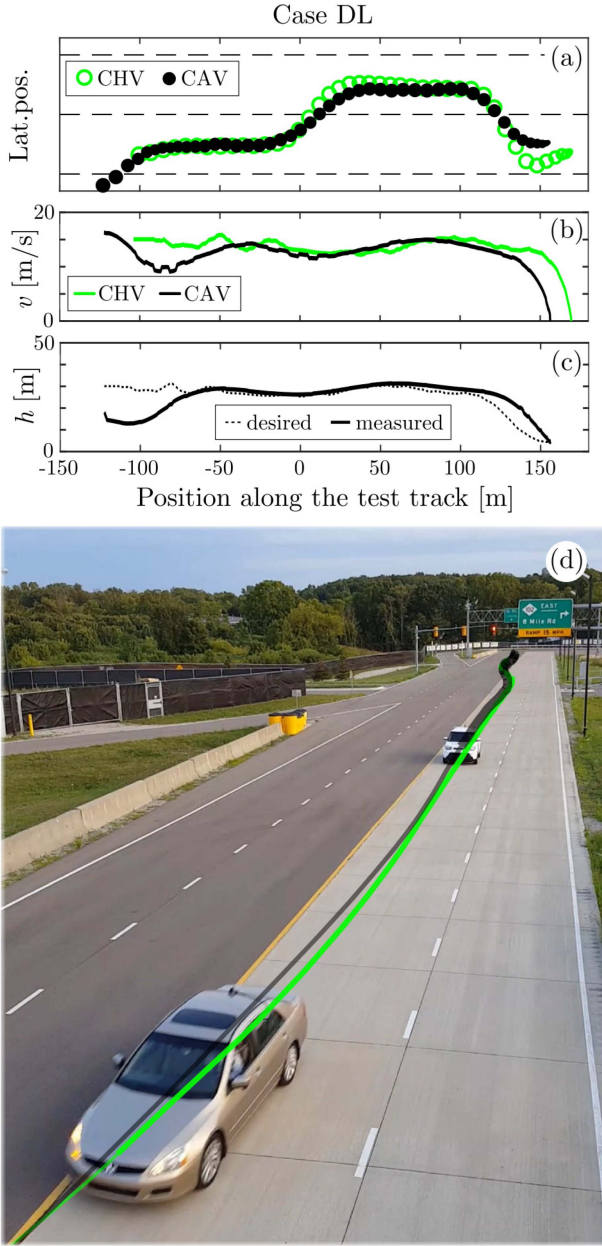


Fig. 13. Connected lane change experiments where the CAV follows the CHV making double lane change similar to the one in Fig. 1. The positions of the CHV (green circles) and the CAV (black dots) are shown in panel (a) along the test track. Sizes of the marks are proportional to the vehicle's speed. Panel (b) shows the speed of the vehicles, while panel (c) depicts the desired headway (thin dashed line) and the measured headway (thick solid line) of the CAV. Picture (d) from the connected double lane change experiments with the trajectories of the CHV (green) and CAV (black) depicted.

$$\begin{aligned}
& -\frac{m \sin \gamma}{\cos^3 \gamma} (V \sin \gamma - \sigma - l\omega) \Omega \dot{\sigma} \\
& + \frac{m}{\cos \gamma} (bV + (l-b)\sigma \sin \gamma) \omega \dot{\omega} \\
& - \frac{ml \sin \gamma}{\cos^3 \gamma} (V \sin \gamma - \sigma - l\omega) \Omega \dot{\omega} + \dots, \quad (37)
\end{aligned}$$

where the terms that do not depend on the pseudo accelerations $\dot{\sigma}$, $\dot{\omega}$ and $\dot{\Omega}$ are not spelled out.

The virtual power of the active forces (i.e., lateral tire forces, self-aligning moments and steering torque) can be calculated as:

$$\begin{aligned}
\delta P = & \left(\frac{F_F}{\cos \gamma} + F_R \right) \delta \sigma + \left(\frac{F_F l}{\cos \gamma} + M_F + M_R \right) \delta \omega \\
& + (M_F + M_S) \delta \Omega, \quad (38)
\end{aligned}$$

where δ refer to virtual quantities. Considering that the virtual power can be given as $\delta P = \Gamma_\sigma \delta \sigma + \Gamma_\omega \delta \omega + \Gamma_\Omega \delta \Omega$, the pseudo forces can be identified:

$$\begin{aligned}
\Gamma_\sigma &= \frac{F_F}{\cos \gamma} + F_R, \\
\Gamma_\omega &= \frac{F_F l}{\cos \gamma} + M_F + M_R, \\
\Gamma_\Omega &= M_F + M_S. \quad (39)
\end{aligned}$$

Then, the Appell-Gibbs equations are obtained as

$$\frac{dA}{d\sigma} = \Gamma_\sigma, \quad \frac{dA}{d\omega} = \Gamma_\omega, \quad \frac{dA}{d\Omega} = \Gamma_\Omega, \quad (40)$$

which can be arranged into the form given in (19) with the elements detailed in (20) and (21).

APPENDIX B TIRE CHARACTERISTICS

Let us consider the so-called brush tire model [45], in which a is the half-length of the tire-ground contact patch, k is the distributed lateral stiffness of the tires, F_z is the vertical load on the axle, μ and μ_0 are the friction coefficients between the tires and the road for sliding and rolling, respectively. Then, the lateral tire force and self-aligning moment can be given as functions of the tire slip angle α :

$$F(\alpha) = \begin{cases} \phi_1 \tan \alpha + \phi_2 \operatorname{sgn} \alpha \tan^2 \alpha \\ \quad + \phi_3 \tan^3 \alpha, & 0 \leq |\alpha| \leq \alpha_{\text{crit}}, \\ \mu F_z \operatorname{sgn} \alpha, & |\alpha| > \alpha_{\text{crit}}, \end{cases} \quad (41)$$

and

$$M(\alpha) = \begin{cases} \mu_1 \tan \alpha + \mu_2 \operatorname{sgn} \alpha \tan^2 \alpha + \mu_3 \tan^3 \alpha \\ \quad + \mu_4 \operatorname{sgn} \alpha \tan^4 \alpha, & 0 \leq |\alpha| \leq \alpha_{\text{crit}}, \\ 0, & |\alpha| > \alpha_{\text{crit}}, \end{cases} \quad (42)$$

respectively. In the formulae, $\alpha_{\text{crit}} = \arctan \frac{3\mu_0 F_z}{2a^2 k}$ corresponds to the critical side-slip angle at which the sliding region expands to the whole contact patch. The coefficients ϕ_i and μ_i can be expressed as

$$\begin{aligned}
\phi_1 &= 2ka^2, \\
\phi_2 &= -\frac{(2ka^2)^2}{3\mu_0 F_z} \left(2 - \frac{\mu}{\mu_0} \right),
\end{aligned}$$

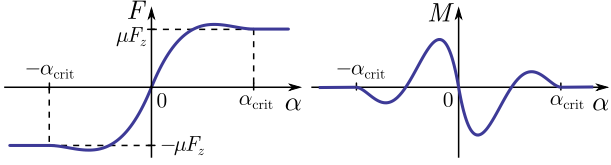


Fig. 14. Lateral tire force F and aligning torque M characteristics as the function of the tire slip angle α .

$$\begin{aligned}
 \phi_3 &= \frac{(2ka^2)^3}{(3\mu_0 F_z)^2} \left(1 - \frac{2\mu}{3\mu_0}\right), \\
 \mu_1 &= -\frac{a}{3}\phi_1, \\
 \mu_2 &= -a\phi_2, \\
 \mu_3 &= -3a\phi_3, \\
 \mu_4 &= a \frac{(2ka^2)^4}{(3\mu_0 F_z)^3} \left(\frac{4}{3} - \frac{\mu}{\mu_0}\right), \quad (43)
 \end{aligned}$$

where the constant $C = 2ka^2$ is often referred to as the cornering stiffness.

The piecewise-smooth continuous functions (41) and (42) are visualized in Fig. 14. For the linear stability analysis of the

rectilinear motion, it is sufficient to use the linear parts for small slip angle α :

$$F(\alpha) \approx \phi_1 \alpha = C\alpha, \quad (44)$$

$$M(\alpha) \approx \mu_1 \alpha = -\frac{a}{3}C\alpha. \quad (45)$$

APPENDIX C

COEFFICIENT MATRICES OF THE LINEAR SYSTEM

The coefficient matrices of the linear system (29) are given by (46)–(48), shown at the bottom of the page.

APPENDIX D

LINEAR STABILITY OF THE LATERAL CONTROLLER

Linear stability charts of the lateral controller detailed in Section IV are constructed in Fig. 15 in the plane of the control gains for the longitudinal speed values $V = 5, 10, 15, 20, 25, 30$ m/s and time delays $\tau_2 = 0.6, 0.7, 0.8, 0.9, 1$ s. The linearly stable domains are shaded. The parameter point A refers to the control gain pairs that was selected as best setup during the experimental stability analysis. This setup was used in Section V for the connected lane change experiments. As shown by the stability charts, this control gain setup is inside the stable domain for all the investigated speed values.

$$\mathbf{M} = \begin{bmatrix} m & mb & 0 & 0 & 0 & 0 & 0 & 0 \\ mb & J_F + J_G + mb^2 & J_F & 0 & 0 & 0 & 0 & 0 \\ 0 & J_F & J_F & 0 & 0 & 0 & 0 & 0 \\ 0 & 0 & 0 & 1 & 0 & 0 & 0 & 0 \\ 0 & 0 & 0 & 0 & 1 & 0 & 0 & 0 \\ 0 & 0 & 0 & 0 & 0 & 1 & 0 & 0 \\ 0 & 0 & 0 & 0 & 0 & 0 & 1 & 0 \\ 0 & 0 & 0 & 0 & 0 & 0 & 0 & 1 \end{bmatrix}, \quad \mathbf{B}_\tau = \begin{bmatrix} 0 & 0 & 0 & 0 & 0 & 0 & 0 & 0 \\ 0 & 0 & 0 & 0 & 0 & 0 & 0 & 0 \\ k_\theta k_d / V & 0 & 0 & 0 & 0 & 0 & 0 & 0 \\ 0 & 0 & 0 & 0 & 0 & 0 & 0 & 0 \\ 0 & 0 & 0 & 0 & 0 & 0 & 0 & 0 \\ 0 & 0 & 0 & 0 & 0 & 0 & 0 & 0 \\ 0 & 0 & 0 & 0 & 0 & 0 & 0 & 0 \\ 0 & 0 & 0 & 0 & 0 & 0 & 0 & 0 \end{bmatrix}, \quad (46)$$

$$\mathbf{A}_0 = \begin{bmatrix} \frac{4ka^2}{V} & \frac{2ka^2 l}{V} + mV & 0 & 0 & 0 & 0 & -2ka^2 & 0 \\ \frac{2ka^2(3l+2a)}{3V} & \frac{2ka^2 l(3l+a)}{3V} + mbV & 0 & 0 & 0 & 0 & -\frac{2ka^2(3l+a)}{3} & 0 \\ \frac{2ka^3}{3V} & \frac{2ka^3 l}{3V} & k_d & 0 & 0 & 0 & k_p - \frac{2ka^3}{3} & -k_i \\ 0 & 0 & 0 & 0 & 0 & 0 & 0 & 0 \\ -1 & 0 & 0 & 0 & 0 & -V & 0 & 0 \\ 0 & -1 & 0 & 0 & 0 & 0 & 0 & 0 \\ 0 & 0 & -1 & 0 & 0 & 0 & 0 & 0 \\ 0 & 0 & 0 & -1 & 0 & 0 & 0 & 0 \\ 0 & 0 & 0 & 0 & 0 & 0 & 1 & 0 \end{bmatrix}, \quad (47)$$

$$\mathbf{A}_\tau = \begin{bmatrix} 0 & 0 & 0 & 0 & 0 & 0 & 0 & 0 \\ 0 & 0 & 0 & 0 & 0 & 0 & 0 & 0 \\ k_y k_d + k_\theta k_p / V & k_\theta k_d & 0 & 0 & k_y k_p & k_\theta k_p + k_y k_d V & 0 & 0 \\ 0 & 0 & 0 & 0 & 0 & 0 & 0 & 0 \\ 0 & 0 & 0 & 0 & 0 & 0 & 0 & 0 \\ 0 & 0 & 0 & 0 & 0 & 0 & 0 & 0 \\ 0 & 0 & 0 & 0 & 0 & 0 & 0 & 0 \\ k_\theta / V & 0 & 0 & 0 & k_y & k_\theta & 0 & 0 \end{bmatrix}. \quad (48)$$

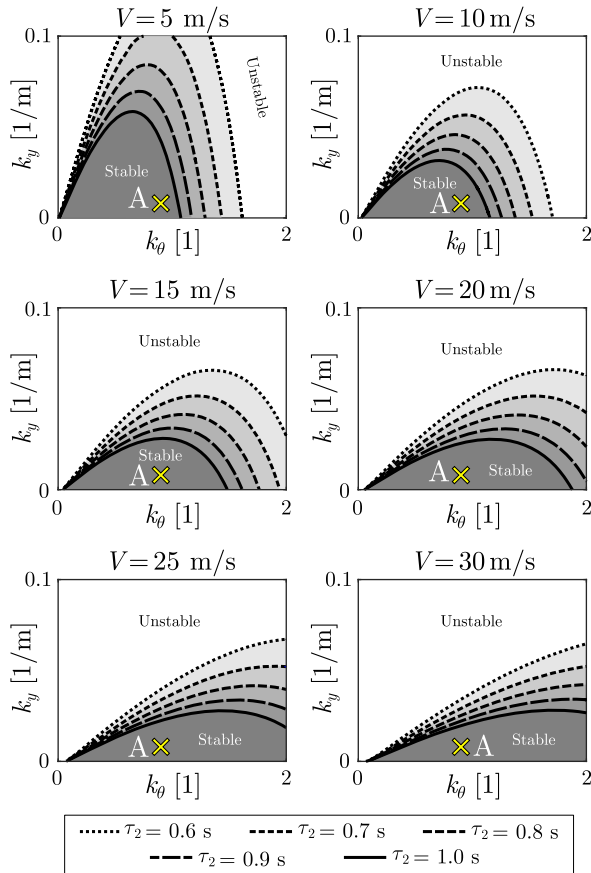


Fig. 15. Linear stability charts of the lateral controller for different longitudinal speed V and time delay τ_2 . Shaded domains refer to linearly stable motion.

ACKNOWLEDGMENT

Denes Takacs would like to thank the Rosztoczy Foundation for their generous support.

REFERENCES

- [1] J. Guanetti, Y. Kim, and F. Borrelli, "Control of connected and automated vehicles: State of the art and future challenges," *Annu. Rev. Control*, vol. 45, pp. 18–40, 2018.
- [2] K. Yoneda, N. Sugauma, R. Yanase, and M. Aldibaja, "Automated driving recognition technologies for adverse," *IATSS Res.*, vol. 43, no. 4, pp. 253–262, 2019.
- [3] C. Corchero and M. Sanmarti, "Vehicle-to-everything (V2X): Benefits and barriers," in *Proc. 15th Int. Conf. Eur. Energy Market*, 2018, pp. 1–4.
- [4] G. Orosz, J. I. Ge, C. R. He, S. S. Avedisov, W. B. Qin, and L. Zhang, "Seeing beyond the line of site-controlling connected automated vehicles," *ASME Dyn. Syst. Control Mag.*, vol. 5, no. 4, pp. S8–S12, 2017.
- [5] FCC, "Dedicated short range communications (DSRC) service," 2016. [Online]. Available: <https://www.fcc.gov/dedicated-short-range-communications-dsrc-service>
- [6] SAE J2735, "Dedicated short range communications (DSRC) message set dictionary set," SAE Int., Tech. Rep. J2735, 2016.
- [7] S. E. Li et al., "Dynamical modeling and distributed control of connected and automated vehicles: Challenges and opportunities," *IEEE Intell. Transp. Syst. Mag.*, vol. 9, no. 3, pp. 46–58, Jul. 2017.
- [8] K. Raboy, J. Ma, E. Leslie, and F. Zhou, "A proof-of-concept field experiment on cooperative lane change maneuvers using a prototype connected automated vehicle testing platform," *J. Intell. Transp. Syst.*, vol. 25, no. 1, pp. 77–92, 2021.
- [9] Z. Wang, G. Wu, and M. Barth, "Distributed consensus-based cooperative highway on-ramp merging using V2X communications," in *Proc. SAE Tech. Paper*, 2018, p. 2018-01-1177.
- [10] S. D. Kumaravel, A. A. Malikopoulos, and R. Ayyagari, "Decentralized cooperative merging of platoons of connected and automated vehicles at highway on-ramps," in *Proc. Amer. Control Conf.*, 2021, pp. 2055–2060.
- [11] D. Bevely et al., "Lane change and merge maneuvers for connected and automated vehicles: A survey," *IEEE Trans. Intell. Veh.*, vol. 1, no. 1, pp. 105–120, Mar. 2016.
- [12] B. Li, Y. Zhang, Y. Feng, Y. Zhang, Y. Ge, and Z. Shao, "Balancing computation speed and quality: A decentralized motion planning method for cooperative lane changes of connected and automated vehicles," *IEEE Trans. Intell. Veh.*, vol. 3, no. 3, pp. 340–350, Sep. 2018.
- [13] J. I. Ge, S. S. Avedisov, C. R. He, W. B. Qin, M. Sadeghpour, and G. Orosz, "Experimental validation of connected automated vehicle design among human-driven vehicles," *Transp. Res. Part C*, vol. 91, pp. 335–352, 2018.
- [14] Y. Wang, N. Bian, L. Zhang, and H. Chen, "Coordinated lateral and longitudinal vehicle-following control of connected and automated vehicles considering nonlinear dynamics," *IEEE Control Syst. Lett.*, vol. 4, no. 4, pp. 1054–1059, Oct. 2020.
- [15] S. Wen and G. Guo, "Control of leader-following vehicle platoons with varied communication range," *IEEE Trans. Intell. Veh.*, vol. 5, no. 2, pp. 240–250, Jun. 2020.
- [16] T. G. Molnár, W. B. Qin, T. Insperger, and G. Orosz, "Application of predictor feedback to compensate time delays in connected cruise control," *IEEE Trans. Intell. Transp. Syst.*, vol. 19, no. 2, pp. 545–559, Feb. 2018.
- [17] H. T. Sykora, M. Sadeghpour, J. I. Ge, D. Bachrathy, and G. Orosz, "On the moment dynamics of stochastically delayed linear control systems," *Int. J. Robust Nonlinear Control*, vol. 30, no. 18, pp. 8074–8097, 2020.
- [18] M. di Bernardo, A. Salvi, and S. Santini, "Distributed consensus strategy for platooning of vehicles in the presence of time-varying heterogeneous communication delays," *IEEE Trans. Intell. Transp. Syst.*, vol. 16, no. 1, pp. 102–112, Feb. 2015.
- [19] G. Orosz, "Connected cruise control: Modelling, delay effects, and nonlinear behaviour," *Veh. Syst. Dyn.*, vol. 54, no. 8, pp. 1147–1176, 2016.
- [20] L. Zhang and G. Orosz, "Motif-based design for connected vehicle systems in presence of heterogeneous connectivity structures and time delays," *IEEE Trans. Intell. Transp. Syst.*, vol. 17, no. 6, pp. 1638–1651, Jun. 2016.
- [21] A. D. Ames, J. W. Grizzle, and P. Tabuada, "Control barrier function based quadratic programs with application to adaptive cruise control," in *Proc. 53rd IEEE Conf. Decis. Control*, 2014, pp. 6271–6278.
- [22] C. R. He and G. Orosz, "Safety guaranteed connected cruise control," in *Proc. 21st IEEE Int. Conf. Intell. Transp. Syst.*, 2018, pp. 549–554.
- [23] T. Ersal et al., "Connected and automated road vehicles: State of the art and future challenges," *Veh. Syst. Dyn.*, vol. 58, no. 5, pp. 672–704, 2020.
- [24] S. Feng, Y. Zhang, S. E. Li, Z. Cao, H. X. Liu, and L. Li, "String stability for vehicular platoon control: Definitions and analysis methods," *Annu. Rev. Control*, vol. 47, pp. 81–97, 2019.
- [25] J. Ploeg, N. van de Wouw, and H. Nijmeijer, " L_p string stability of cascaded systems: Application to vehicle platooning," *IEEE Trans. Control Syst. Technol.*, vol. 22, no. 2, pp. 786–793, Mar. 2014.
- [26] J. Monteil, G. Russo, and R. Shorten, "On L_∞ string stability of nonlinear bidirectional asymmetric heterogeneous platoon systems," *Automatica*, vol. 105, pp. 198–205, 2019.
- [27] D. Hajdu, J. I. Ge, T. Insperger, and G. Orosz, "Robust design of connected cruise control among human-driven vehicles," *IEEE Trans. Intell. Transp. Syst.*, vol. 21, no. 2, pp. 749–761, Feb. 2020.
- [28] C. R. He, J. I. Ge, and G. Orosz, "Fuel efficient connected cruise control for heavy-duty trucks in real traffic," *IEEE Trans. Control Syst. Technol.*, vol. 28, no. 6, pp. 2474–2481, Nov. 2020.
- [29] S. S. Avedisov, G. Bansal, and G. Orosz, "Impacts of connected automated vehicles on freeway traffic patterns at different penetration levels," *IEEE Trans. Intell. Transp. Syst.*, to be published, doi: [10.1109/TITS.2020.3043323](https://doi.org/10.1109/TITS.2020.3043323).
- [30] J. Jiang and A. Astolfi, "Lateral control of an autonomous vehicle," *IEEE Trans. Intell. Veh.*, vol. 3, no. 2, pp. 228–237, 2018.
- [31] J. Wurts, J. L. Stein, and T. Ersal, "Collision imminent steering at high speeds on curved roads using one-level nonlinear model predictive control," *IEEE Access*, vol. 9, pp. 39 292–39 302, 2020.
- [32] J. Y. Goh, T. Goel, and J. C. Gerdes, "Toward automated vehicle control beyond the stability limits: Drifting along a general path," *J. Dynamic Syst., Meas., Control*, vol. 142, no. 2, 2019, Art. no. 0 21004.
- [33] P. Hingwe, H.-S. Tan, A. K. Packard, and M. Tomizuka, "Linear parameter varying controller for automated lane guidance: Experimental study on tractor-trailers," *IEEE Trans. Control Syst. Technol.*, vol. 10, no. 6, pp. 793–806, Nov. 2002.

- [34] S. Xu and H. Peng, "Design, analysis, and experiments of preview path tracking control for autonomous vehicles," *IEEE Trans. Intell. Transp. Syst.*, vol. 21, no. 1, pp. 48–58, Jan. 2020.
- [35] P. Falcone, F. Borrelli, J. Asgari, H. E. Tseng, and D. Hrovat, "Predictive active steering control for autonomous vehicle systems," *IEEE Trans. Control Syst. Technol.*, vol. 15, no. 3, pp. 566–580, May 2007.
- [36] P. Anistratov, B. Olofsson, and L. Nielsen, "Lane-deviation penalty formulation and analysis for autonomous vehicle avoidance maneuvers," in *Proc. Inst. Mech. Eng., Part D, J. Automobile Eng.*, vol. 235, no. 12, pp. 3036–3050, 2021.
- [37] S. Di Cairano, H. Tseng, D. Bernardini, and A. Bemporad, "Steering vehicle control by switched model predictive control," *IFAC Proc. Volumes*, vol. 43, no. 7, pp. 1–6, 2010.
- [38] F. Gantmacher, *Lectures in Analytical Mechanics*. Moscow, Russia: MIR Publishers, 1975.
- [39] V. De Sapio, *Advanced Analytical Dynamics: Theory and Applications*. Cambridge, UK: Cambridge Univ. Press, 2017.
- [40] S. Bae *et al.*, "Cooperation-aware lane change maneuver in dense traffic based on model predictive control with recurrent neural network," *Amer. Control Conf.*, pp. 1209–1216, 2020.
- [41] S. Beregi, D. Takács, C. R. He, S. S. Avedisov, and G. Orosz, "Hierarchical steering control for a front wheel drive automated car," *14th IFAC Workshop Time Delay Syst. (TDS)*, vol. 51, no. 14, pp. 1–6, 2018.
- [42] G. Stépán, *Retarded Dynamical Systems*. Harlow, UK: Longman, 1989.
- [43] T. Insperger and G. Stépán, *Semi-Discretisation for Time-Delay Systems*. New York, NY, USA: Springer, 2011.
- [44] L. N. Trefethen, *Spectral Methods in Matlab*. Philadelphia, PA, USA: SIAM, 2000.
- [45] H. Pacejka, *Tire and Vehicle Dynamics*. Oxford, UK: Elsevier, 2012.



Sándor Beregi is graduated from the Budapest University of Technology and Economics, Budapest, Hungary, as a Mechanical Engineer. He received the bachelor's and master's degrees in 2013 and 2015, respectively. He received the Ph.D. thesis titled 'Delay effects and non-smoothness in the dynamic tyre-road contact and vehicle steering' in 2020. From 2018 to 2019, he was an Assistant Research Fellow with the MTA-BME Research Group on Dynamics of Machines and Vehicles in Budapest, Budapest, Hungary. Since 2019, he has been a Research Associate with the

University of Bristol, Bristol, U.K. His research interests include tire and vehicle dynamics, nonlinear dynamical systems, experimental bifurcation analysis and time-delay systems.



Sergei S. Avedisov received the M.Sc. and Ph.D. degrees in mechanical engineering from the University of Michigan, Ann Arbor, MI, USA, in 2016 and 2019, respectively. His research interests included longitudinal and lateral control of connected automated vehicles. He is currently working with Toyota R&D InfoTech Labs as a Connected Automated Driving Engineer.



Chaozhe R. He received the B.Sc. degree in applied mathematics from the Beijing University of Aeronautics and Astronautics, Beijing, China, in 2012, the M.Sc. and Ph.D. degrees in mechanical engineering from the University of Michigan, Ann Arbor, MI, USA, in 2015 and 2018, respectively. Dr. He is with Plus.ai Inc. and is working on planning and control algorithm development. His research interests include dynamics and control of connected automated vehicles, optimal and nonlinear control theory, and data-driven control.



Dénes Takács received the M.Sc. and Ph.D. degrees in mechanical engineering from the Budapest University of Technology and Economics, Budapest, Hungary, in 2005 and 2011, respectively. Between 2011 and 2018, he was with the MTA-BME Research Group on Dynamics of Machines and Vehicles in Budapest, Hungary. Since 2018, he is an Associate Professor with the Budapest University of Technology and Economics, Budapest, Hungary. His research interests include tire and vehicle dynamics, nonlinear dynamics and time-delay systems.



Gábor Orosz received the M.Sc. degree in engineering physics from the Budapest University of Technology, Budapest, Hungary, in 2002, and the Ph.D. degree in engineering mathematics from the University of Bristol, Bristol, U.K., in 2006. He held Postdoctoral Positions with the University of Exeter, Exeter, U.K., and with the University of California, Santa Barbara, CA, USA. In 2010, he joined the University of Michigan, Ann Arbor, MI, USA, where he is currently an Associate Professor in mechanical engineering and in civil and environmental engineering.

His research interests include nonlinear dynamics and control, time delay systems, and learning with applications to connected and automated vehicles, traffic flow, and biological networks.